Tunable band gaps and optical absorption properties of bent MoS_2 nanoribbons

Hong Tang, Bimal Neupane, Santosh Neupane, Shiqi Ruan, Niraj K. Nepal, and Adrienn Ruzsinszky

Department of Physics, Temple University, Philadelphia, PA 19122

ABSTRACT The large tunability of band gaps and optical absorptions of armchair MoS_2 nanoribbons of different widths under bending is studied using density functional theory and many-body perturbation GW and Bethe-Salpeter equation approaches. We find that there are two critical bending curvatures, and the non-edge and edge band gaps generally show a non-monotonic trend with bending. The non-degenerate edge gap splits show an oscillating feature with ribbon width n, with a period $\Delta n = 3$, due to quantum confinement effects. The complex strain patterns on the bent nanoribbons control the varying features of band structures and band gaps that result in varying exciton formations and optical properties. The binding energy and the spin singlet-triplet split of the exciton forming the lowest absorption peak generally decrease with bending curvatures. The large tunability of optical properties of bent MoS_2 nanoribbons is promising and will find applications in tunable optoelectronic nanodevices.

Atomically thin two-dimensional (2D) layered materials, such as graphene and transition metal (di or mono) chalcogenides, are drawing a great attention in material science.[1-6] They are light weight and flexible, yet with a relatively high mechanical strength. They can be tailored into different shapes, intercalated by other atoms and molecules, strained in-plane, bent out-of-plane, rolled up into scrolls, wrinkled or folded in the 2D plane, and conformed onto a nanoscale-patterned substrate,[7] achieving varied, controllable properties. Additionally, they can be assembled, through interlayer van der Waals interactions,[8] into layer-on-layer stacked or twisted homo- or heterostructures, such as moire[9,10] patterned layered materials, leading to unprecedented, amazing properties. They are bestowed with a great promise in applications for next generation nanoelectronics[11] and optoelectronics.[4]

The reduced dimensionality in 2D materials usually results in reduced dielectric screening and enhanced electron-electron interactions,[12-15] and hence large exciton effects, which may largely enhance the optical properties of 2D materials. Molybdenum disulfide (MoS_2) is a typical transition-metal dichalcogenide (TMD), featuring a high electron mobility comparable to graphene and a finite energy gap.[16] When decreasing the thickness from a bulk form down to a monolayer, MoS_2 crosses over from an indirect gap semiconductor to a direct one, as a result of inversion symmetry breaking in its honeycomb lattice structure.[2,12] Optical absorption and photoluminescence[12,17] determine the optical band gap of monolayer (1L) MoS_2 as 1.8~1.9eV, while its fundamental band gap (or electronic band gap) is found to be ~2.5eV by the delicate photocurrent[18] and scanning tunnelling spectroscopy[19] experiments, confirming the large binding energy (>570meV) of the exciton in 1L MoS_2 systems. Qiu et al.[20] elaborately investigated the optical spectrum of 1L MoS_2 by using the GW+BSE[21] (Bethe-Salpeter equation) approach and revealed a large number and diverse character of bound excitons in it, suggesting its potential applications to electronics utilizing inter- and intraexcitonic processes.

In terms of strain engineering,[22,23] it has been demonstrated that strain particularly plays an important role in manipulating the electronic and optical properties of graphene and TMDs. Strains change the relative

positions of atoms, local potentials, and the orbital overlap between the metal and chalcogen atoms, resulting in significant alterations of electronic properties. At a homogeneous (or uniform) uniaxial strain ~2%, 1L MoS_2 changes from direct to indirect bandgap semiconductor, while with a biaxial tensile strain 10–15%, it undergoes a semiconductor-to-metal phase transition.[24-26] Since large homogeneous uniaxial or biaxial strains are relatively harder to realize in practical devices,[27] local nonuniform strains (LNS), by wrinkling,[23,28,29] indentation and interface conforming,[30,31] have been explored recently. Interestingly, LNS can generate novel effects, such as the exciton funnel,[23] in which before recombination excitons drift to lower bandgap regions caused by higher local strains, and spontaneous emission enhancement,[32] which is explored for ultracompact single-photon quantum light emitters.

Mechanical bending can provide effective LNS on nanoribbons, as shown by Yu et al.[33] on the bending effects for MoS_2 and phosphorene nanoribbons. It was found that the bending induced shifting of edge bands and the charge localization of top valence bands can mitigate or remove the Fermi-level pinning and change the conductivity both along and perpendicular to the width direction of doped nanoribbons. Since edge band positions in band structures and edge band gaps are important for the optical absorption of nanoribbons, it is appealing to show how the edge bands will evolve with bending for varied widths of nanoribbons and how this will modify the optical properties. In this work, with density functional theory (DFT)[34-39] and many-body perturbation G_0W_0 computations,[40,41] we systematically investigate the band structures and band gaps of semiconducting armchair 1L MoS_2 nanoribbons with widths from 1.3 to 3.6 nm under different bending curvatures. It is found that the evolution of the edge gap has more features and shows a nonmonotonic trend with bending curvatures. The phenomenon is correlated with the complex strain patterns experienced in the bent nanoribbons. Furthermore, we use the GW+BSE[21] approach to calculate the optical absorption spectra and reveal a large tunability of optical absorption by bending nanoribbons. Computer codes and computational parameters are presented in the Supporting Information.

Band gap tunability. The nanoribbon (denoted as A*n*MoS_2) is formed by cutting from monolayer hexagonal (1H) MoS_2 and its two armchair edges are hydrogen passivated (Figure 1a-1c). *n* represents the number of MoS_2 units in one repeating unit along axis z. We study A*n*MoS_2 nanoribbons with *n* from 9 to 24 and widths from 1.3nm to 3.6nm. The band structures of nanoribbons show a large tunability with bending. As shown for A13MoS_2 (Figure 1d), with an increase in bending curvature κ ($\kappa = 1/\mathrm{R}$, where R is an average curvature radius, Supporting Figure S1), the two nearly degenerate conduction bands C1 and C2 slowly approach to the Fermi energy, while the two valence bands V1 and V2 approach to the valence band continuum (VBC) and eventually merge into it at $\mathrm{R} = 10$Å. C1, C2, V1 and V2 are mostly developed from the *d* orbitals of the edge Mo atoms.[42] Both EG (edge band gap, see Figure 1e and caption) and NEG (non-edge band gap, Figure 1f) can change up to or over 50% with bending curvatures. There are two critical curvatures, namely κ_{c1} and κ_{c2}. For A13MoS_2, $\kappa_{c1} = 0.0625/$Å ($\mathrm{R} = 16$Å) and $\kappa_{c2} = 0.100/$Å ($\mathrm{R} = 10$ Å). With curvatures from zero to κ_{c1}, denoted as Region I, EG generally decreases, while NEG increases. In Region II, denoted as the range from κ_{c1} to κ_{c2}, EG remains nearly constant. With curvatures larger than κ_{c2}, denoted as Region III, EG decreases. Both in Regions II and III, NEG decreases. At κ_{c1}, the border line between Regions I and II, NEG shows a hump (maximum). At κ_{c2}, V1 and V2 merge into VBC and EG turns to a quick decrease. All nanoribbons A*n*MoS_2 with *n* from 12 to 23 show similar features (Supporting Figure S2). However, with increasing width (larger *n*), both κ_{c1} and κ_{c2} become smaller and Regions I and II gradually merge, and the NEG hump feature is reducing. Eventually, for A24MoS_2, EG shows nearly a constant behavior followed by a decrease with curvatures, while NEG shows a monotonic decrease. The strains in bent nanoribbons are highly non-uniform, complex, and closely related to the observed tunability of band gaps. For A13MoS_2, the strain in the xy-plane (Supporting note, Figures S4-S6) reaches the maximal compression up to the critical $\kappa_{c1} = 0.0625/$Å ($\mathrm{R} = 16$Å), while the strain along

the z direction reaches the maximal expansion at this κ_{c1}. This delicately changes the local potentials and orbital overlaps and construes the hump feature of NEG vs. curvatures. (See the details of evolutions of strain patterns in bent nanoribbons in Supporting Figures S5-S9)

Non-degenerate splits of edge bands. The PBE value of NEG of flat nanoribbon shows a monotonic decrease with widths and almost reaches 1.7eV (the PBE value of monolayer MoS_2) at A24MoS_2, while EG shows a vibrating feature with widths with a period $\Delta n = 3$ (Figure 2). For flat nanoribbons, the same period $\Delta n = 3$ is shown for the non-degenerate splits of edge bands (Figure 2), namely, $\Delta E_C = E_{C2} - E_{C1}$, the energy difference between C2 and C1 at the Γ point, and $\Delta E_V = E_{V1} - E_{V2}$, the energy difference between V1 and V2 at the Γ point. For flat nanoribbons A$n$$MoS_2$ with n = 9, 12, 15, 18, 21, and 24 (i.e., $n = 3p$, where p is an integer), both ΔE_C and ΔE_V are minimal, showing nearly degenerate edge bands. However, the flat nanoribbons with other n values show non-degenerate edge bands around the Γ point, with larger ΔE_C and ΔE_V for narrower nanoribbons (smaller n). For the same nanoribbon, ΔE_V is approximately three times ΔE_C. Note that the flat nanoribbons with widths $n = 3p$ have larger EG values than those of neighboring n's (Figure 2). This differs from the previous study[43] of $n = 3p - 1$ with non-hydrogen passivated nanoribbons. Hydrogen passivation does not change the oscillating feature of EG with widths n, but shifts the maximum n's by +1. The non-degenerate splits ΔE_C and ΔE_V are robustly kept when bending is applied. For example, for A13MoS_2, the split ΔE_V is kept from R = ∞ to 11Å, until V1 and V2 merge into VBC at R = 10 Å (Supporting Figure Set S1). Bending can even enhance the split ΔE_V, as can be seen for A11MoS_2 (Supporting Figure Set S15) with R = ∞ to 11Å, and induce the split ΔE_V, as can be seen for A12MoS_2 (Supporting Figure Set S16) with R = 16 to 10Å. The splits ΔE_C and ΔE_V on flat nanoribbons may be due to the quantum confinement effect along the width direction. Bending can couple with the quantum confinement effect and enhances the splits, especially for narrower nanoribbons.

Tunable optical properties. The complex strain patterns in the bent nanoribbons control the varying features of band gaps. Those features will result in varying exciton formations and optical properties. To elucidate the tunable optical absorptions of bent nanoribbons, we calculate the absorption spectra with GW+BSE for nanoribbons with bending curvatures in the three curvature regions (I, II and III). The calculated optical absorption spectra of A13MoS_2 nanoribbon are shown in Figure 3, showing a large tunability of absorption with bending curvatures. The absorption peaks are generally shifted to lower energies and more absorption peaks occur. For example, there is almost no absorption at photon energies 0.35 and 1.25 eV for a flat ribbon, while the bent nanoribbon with R = 6 Å produces a weak absorption peak at 0.35eV and a strong peak at 1.25eV. With increasing curvatures, the quasiparticle gap of the nanoribbon decreases (Table 1), more and more bright exciton states appear within the energy range below the fundamental gap, and the bending nanoribbon shows a broad absorption within this energy range.

At R = ∞ (flat), peak A′ consists of two degenerate (energy difference < 3meV) exciton states at energy 0.57 eV, and each of them is due to a combination of four transitions, namely, V1 to C1, V1 to C2, V2 to C1, and V2 to C2, mainly around the Γ point. The wavefunction of the exciton is shown in Figure 4. The binding energy of these excitons is 1.41 eV, which is bigger than that (0.96 eV [20]) of the lowest exciton in 1L MoS_2, due to the further reduced screening and enhanced electron-electron interaction in the one-dimensional nanoribbon. Peak B′ mainly consists of two degenerate exciton states at 0.94 eV. One is mainly due to the transition around Γ from V3 to C1, and the other from V3 to C2. There are two degenerate and relatively weak exciton states at 1.01 eV, merged in the right bottom of peak B′. They are the excited states of the excitons forming peak A′. Peak C′ consists of two sets of exciton sates. The first set, with an energy at 1.11 eV, is two degenerate exciton states mainly corresponding to the transition V4 to C1 (or V4 to C2) around Γ, while the second set, with a slightly higher energy at 1.17 eV, is two degenerate exciton states

mainly due to V3 to C1 (or V3 to C2) around k points slightly away from, but near Γ. The wavefunction of this second set exciton has a nodal feature, indicating that it is the excited state of the exciton forming peak B′ at 0.94 eV. Peaks D′ and E′ are relatively weak and mainly due to transitions from lower valence bands (V5 or V6) to upper edge bands (C1 or C2), and their wavefunctions in k space have more complex nodal features. Peak F′ is mainly due to transition V1→C3 around Γ. This exciton has an energy very close to the fundamental gap and hence a small binding energy of 0.09 eV.

At $R = 13Å$, the excitonic composition of peak A′′ is similar to that of peak A′. However, due to bending, the two originally degenerate exciton states red shift to 0.5 and 0.55 eV, respectively. This makes the overall peak A′′ broadened and located at a lower energy than peak A′. Peak B′′ becomes complex. Overall, it is still similar to peak B′, and consists of exciton states corresponding to transitions around Γ from V3 to C1 (or V3 to C2), and the excited states of excitons forming peak A′′. The overall peak position of B′′ red shifts, compared to peak B′. Similarly, peaks C′′ to G′′ are complex and involve mixtures of transitions involving lower valence bands (V3 to V6) and upper edge bands (C1 and C2).

At $R = 9Å$, peaks A′′′ and B′′′ are, respectively, due to two excitons, everyone of which is mainly from the mixed transitions involving V2→C1, V3→C1, V2→C2, and V3→C2 around Γ. The exciton corresponding to peak A′′′ is at 0.5 eV, while the one for B′′′ is at 0.57 eV, and the energy difference may be mainly due to bending effects. Peaks A′′′ and B′′′ are related to, but different with peaks A′ and A′′. At $R = 9Å$, the lower edge bands V1 and V2 are already merged into VBC. As can be seen (Supporting Figure S21), V1, V2 and V3 are very close to each other around Γ, and V2 and V3 have a slightly larger dispersion than V1 around Γ. This may explain why transitions V1→C1/C2 don't have large contributions (<4%) to peaks A′′′ and B′′′. In fact, the exciton states corresponding to transitions V1→C1/C2 are moved to 0.65 and 0.7 eV, and are relatively weak and embedded in the valley between B′′′and C′′′. Peaks C′′′, D′′′ and E′′′ form a broad composite peak and consist of many exciton states involving mixed transitions from V1, V2 and V3 to C1 and C2. Some of these excitons bear features of the excited states of the excitons forming peaks A′′′ and B′′′. Peaks F′′′ and G′′′ are weak and involve transitions from lower valence bands (V4, V5, and V6) to C1 and C2. Peak H′′′, similar to peak F′, is mainly due to exciton states involving transitions from V1, V2, V3 to C3, since V1, V2, and V3 are very close around Γ. The binding energy of the exciton states mainly contributing to peak H′′′ is 0.24 eV, larger than that for peak F′.

At $R = 6Å$, the main contribution to peak A′′′′ is two degenerate excitons at 0.33 eV and they are mainly due to transitions V1/V2→C1/C2 around Γ. This is mainly due to the closeness of V1 and V2 around Γ, and V3 is lower than V1 and V2 there (Supporting Figure S21). Peak B′′′′ is mainly due to excitons of transitions V3→C1/C2 and V4→C1/C2. Peaks from C′′′′ to I′′′′ become more complex. The bending lowers EG, and the conduction band continuum (CBC) also shifts downwards. This makes the upper edge bands C1 and C2 closer to CBC, and more transitions relating lower valence bands (V3, V4, V5, etc.) and higher conduction bands (C3, C4, etc.) occur. For example, peak G′′′′ has contributions of excitons involving mixed transitions from V3-V5 to C1-C4.

The A12MoS_2 nanoribbon also has similar tunable properties (Supporting Figure S22). With increasing curvature, the main absorption peaks shift to lower frequencies and become broader. Bending activates more exciton states and many of them contribute to the optical absorptions. The lowest energy exciton's binding energy generally decreases with bending (Table 1), basically consistently with an increase in the static dielectric constant (Supporting Figures S23 and S24) with bending, while the wavefunction distortions induced by the bending surface (or space) in bent nanoribbons may also influence the binding. The spin singlet-triplet splitting of the lowest energy exciton is about 0.22eV for flat ribbons and shows a tunability (decrease) with bending (Table 1). The bending space reduces the overlap between electron and

hole wave functions and thus results in a decrease in e–h exchange interactions. We think that the edge states in the nanoribbons have similar properties as those of the defect states[44] in monolayer TMDs and the relatively large and tunable singlet-triplet splitting can make the nanoribbon system suitable for quantum information applications.[45] The large tunability of electron energy loss spectrum and absorption coefficient with bending is shown in Figure 5, consistent with the optical absorption spectra. As shown here, the mechanical bending is an effective means to control and fine tune the optical properties of nanoribbons.

Conclusions. From first-principles calculations DFTs and GW+BSE, we assessed the large tunability of band gaps and optical absorptions of armchair MoS_2 nanoribbons of different widths under different bending curvatures. We find that there are two critical bending curvatures κ_{c1} and κ_{c2} with $\kappa_{c1} < \kappa_{c2}$. Below κ_{c1}, the edge gap slowly decreases with κ, while the non-edge gap slowly increases. From κ_{c1} to κ_{c2}, the edge gap nearly keeps constant, and beyond κ_{c2}, it decreases. From κ_{c2} and on, the lower edge bands merge into the valence band continuum. The non-edge gap decreases from κ_{c1} and on, and has a maximum around κ_{c1}, consistent with the maximum strain along the ribbon length direction around κ_{c1}. For wider nanoribbons (width = 3.6 nm), Regions I and II merge, and the non-edge gap shows a monotonic decrease with bending, while the edge gap shows a constant behavior followed by a decrease under increasing curvatures. The edge gaps and the non-degenerate edge gap splits show an oscillating feature with ribbon width n, with a period $\Delta n = 3$, due to quantum confinement effects. The non-degenerate edge gap splits generally persist with bending. Bending generally induces more exciton states and they contribute to controllable optical absorptions. The induced excitons are related to the bands near the gap and the subtle changes of these bands with bending. The binding energy and the spin singlet-triplet split of the exciton forming the lowest absorption peak generally decreases with bending curvatures. Since MoS_2 nanotubes have already been synthesized,[46,47] it may be feasible to realize the bent nanoribbons by embedding MoS_2 nanotubes into nano-troughs and etching or eroding out some parts of the nanotubes. The large tunability of optical properties of bending MoS_2 nanoribbons is appealing and will find applications in tunable optoelectronic nanodevices.

Supporting Information

Supercell sizes, parameters of DFT and GW+BSE computations; evolutions of NEG and EG for A$n$$MoS_2$ nanoribbons with n from 9 to 24 with bending curvatures; calculation scheme for strains in the xy plane and along the z direction; the evolution of strains with curvature radii for the A11MoS_2, A12MoS_2, and A13MoS_2 nanoribbons; the length of vector c of the supercell as a function of curvatures for nanoribbons A$n$$MoS_2$ with n form 9 to 24; plots of exciton peaks for A13MoS_2 nanoribbon; G_0W_0 band structures of A13MoS_2 nanoribbon under different curvature radii; optical absorption spectra of A12MoS_2 nanoribbon under different curvature radii; real part of dielectric functions, EELS and absorption coefficients of A12MoS_2, A13MoS_2 nanoribbons under different curvature radii; SCAN band structures of Armchair-$n$$MoS_2$ nanoribbon with n from 9 to 24.

Acknowledgement

This material is based upon work supported by the U.S. Department of Energy, Office of Science, Office of Basic Energy Sciences, under Award Number DE-SC0021263. This research used resources of the National Energy Research Scientific Computing Center, a DOE Office of Science User Facility supported by the Office of Science of the U.S. Department of Energy under Contract No. DE-AC02-05CH11231.

References

(1) Butler, S. Z.; Hollen, S. M.; Cao, L.; Cui, Y.; Gupta, J. A.; Gutiérrez, H. R.; Heinz, T. F.; Hong, S. S.; Huang, J.; Ismach, A. F.; Johnston-Halperin, E.; Kuno, M.; Plashnitsa, V. V.; Robinson, R. D.; Ruoff, R. S.; Salahuddin, S.; Shan, J.; Shi, L.; Spencer, M. G.; Terrones, M.; Windl, W.; Goldberger, J. E. Progress, challenges, and opportunities in two-dimensional materials beyond graphene. *ACS Nano* **2013**, *7*, 2898–2926.

(2) Splendiani, A.; Sun, L.; Zhang, Y.; Li, T.; Kim, J.; Chim, C.-Y.; Galli, G.; Wang, F. Emerging Photoluminescence in Monolayer MoS2. *Nano Lett*. **2010**, *10*, 4, 1271–1275.

(3) Chaves, A.; Azadani, J. G.; Alsalman, H.; da Costa, D. R.; Frisenda, R.; Chaves, A. J.; Song, S. H.; Kim, Y. D.; He, D.; Zhou, J.; Castellanos-Gomez, A.; Peeters, F. M.; Liu, Z.; Hinkle, C. L.; Oh, S.-H.; Ye, P. D.; Koester, S. J.; Lee, Y. H.; Avouris, P.; Wang, X.; Low, T. Bandgap engineering of two-dimensional semiconductor materials. *npj 2D Materials and Applications* **2020**, *14*(29).

(4) Chen, P.; Lo, T. W.; Fan, Y.; Wang, S.; Huang, H.; Lei, D.; Chiral Coupling of Valley Excitons and Light through Photonic Spin–Orbit Interactions. *Adv. Opt. Mater.* **2020**, *8*(1901233).

(5) Mounet, N.; Gibertini, M.; Schwaller, P.; Campi, D.; Merkys, A.; Marrazzo, A.; Sohier, T.; Castelli, I. E.; Cepellotti, A.; Pizzi, G.; Marzari, N. Two-dimensional materials from high-throughput computational exfoliation of experimentally known compounds. *Nature Nanotechnology* **2018**, *13*, 246–252.

(6) Mueller, T.; Malic, E. Exciton physics and device application of two-dimensional transition metal dichalcogenide semiconductors. *npj 2D Materials and Applications* **2018**, *2*(29).

(7) Palacios-Berraquero, C.; Kara, D. M.; Montblanch, A. R.-P.; Barbone, M.; Latawiec, P.; Yoon, D.; Ott, A. K.; Loncar, M.; Ferrari, A. C.; Atatüre, M. Large-scale quantum-emitter arrays in atomically thin semiconductors. *Nat. Commun.* **2017**, *8*, 15093.

(8) Geim, A.; Grigorieva, I. Van der Waals heterostructures. *Nature* **2013**, *499*, 419−425.

(9) Cao, Y.; Fatemi, V.; Fang, S.; Watanabe, K.; Taniguchi, T.; Kaxiras, E.; Jarillo-Herrero, P. Unconventional superconductivity in magic-angle graphene superlattices. *Nature* **2018**, *556*, 43.

(10) Luo, Y.; Engelke, R.; Mattheakis, M.; Tamagnone, M.; Carr, S.; Watanabe, K.; Taniguchi, T.; Kaxiras, E.; Kim, P.; Wilson, W. L. In situ nanoscale imaging of moiré superlattices in twisted van der Waals heterostructures. *Nature Commun*. **2020**, *11*, 4209.

(11) Ahn, E. C. 2D materials for spintronic devices. *npj 2D Materials and Applications* **2020**, *4*,17.

(12) Mak, K. F.; Lee, C.; Hone, J.; Shan, J.; Heinz, T. F. Atomically Thin MoS_2: A New Direct-Gap Semiconductor. *Phys. Rev. Lett*. **2010**, *105*, 136805.

(13) Bradley, A. J.; Ugeda, M. M.; da Jornada, F. H.; Qiu, D. Y.; Ruan, W.; Zhang, Y.; Wickenburg, S.; Riss, A.; Lu, J.; Mo, Z.; Hussain, S.-K.; Shen, Z.-X.; Louie, S. G.; Crommie, M. F. *Nano Lett*. **2015**, *15*, 2594−2599.

(14) Kim, J.; Yun, W. S.; Lee, J. D. Optical Absorption of Armchair MoS2 Nanoribbons: Enhanced Correlation Effects in the Reduced Dimension. *J. Phys. Chem. C* **2015**, *119*, 13901−13906.

(15) Li, L.; Kim, J.; Jin, C.; Ye, G. J.; Qiu, D. Y.; da Jornada, F. H.; Shi, Z.; Chen, L.; Zhang, Z.; Yang, F.; Watanabe, K.; Taniguchi, T.; Ren, W.; Louie, S. G.; Chen, X. H.; Zhang, Y.; Wang, F. *Nat. Nanotechnol*. **2017**, *12*, 21−25.

(16) Radisavljevic, B.; Radenovic, A.; Brivio, J.; Giacometti, V. ; Kis, A. Single-layer MoS2 transistors. *Nat. Nanotechnol*. **2011**, *6*, 147–150.

(17) Tongay, S.; Zhou, J.; Ataca, C.; Lo, K.; Matthews, T. S.; Li, J.; Grossman, J. C.; Wu, J. Thermally Driven Crossover from Indirect toward Direct Bandgap in 2D Semiconductors: MoSe2 versus MoS2. *Nano Lett.* **2012**, *12*, 5576.

(18) Klots, A. R.; Newaz, A. K. M.; Wang, B.; Prasai, D.; Krzyzanowska, H.; Lin, J.; Caudel, D.; Ghimire, N. J.; Yan, J.; Ivanov, B. L.; Velizhanin, K. A.; Burger, A.; Mandrus, D. G.; Tolk, N. H.; Pantelides, S. T.; Bolotin, K. I. Probing excitonic states in suspended two-dimensional semiconductors by photocurrent spectroscopy. *Sci. Rep.* **2014**, *4*, 6608.

(19) Huang, Y. L.; Chen, Y. Zhang, W.; Quek, S. Y.; Chen, C.-H.; Li, L.-J.; Hsu, W.-T.; Chang, W.-H.; Zheng, Y. J.; Chen, W.; Wee, A. T. S. Bandgap tunability at single-layer molybdenum disulphide grain boundaries. *Nat Commun*. **2015**, *6*, 6298.

(20) Qiu, D. Y.; da Jornada, F. H.; Louie, S. G. Optical Spectrum of MoS_2: Many-Body Effects and Diversity of Exciton States. *Phys. Rev. Lett*. **2013**, *111*, 216805.

(21) Rohlfing, M.; Louie, S. G. Electron-hole excitations and optical spectra from first principles. *Phys. Rev. B* **2000**, *62*, 4927.

(22) Peng, Z.; Chen, X.; Fan, Y.; Srolovitz, D. J.; Lei, D. Strain engineering of 2D semiconductors and graphene: from strain fields to band-structure tuning and photonic applications. *Light: Science & Applications* **2020**, *9*, 190.

(23) Castellanos-Gomez, A.; Roldán, R.; Cappelluti, E.; Buscema, M.; Guinea, F.; van der Zant, H. S. J.; Steele, G. A. Local strain engineering in atomically thin MoS2. *Nano Lett*. **2013**, *13*, 5361–5366.

(24) Scalise, E.; Houssa, M.; Pourtois, G.; Afanasev, V.; Stesmans, André. Strain-induced semiconductor to metal transition in the two-dimensional honeycomb structure of MoS2. *Nano Res.* **2012**, *5*, 43–48.

(25) Feng, J.; Qian, X.; Huang, C.-W.; Li, J. Strain-engineered artificial atom as a broad-spectrum solar energy funnel. *Nat. Photonics* **2012**, *6*, 866–872.

(26) Ghorbani-Asl, M.; Borini, S.; Kuc, A.; Heine, T. Strain-dependent modulation of conductivity in single-layer transition-metal dichalcogenides. *Phys. Rev. B* **2013**, *87*, 235434.

(27) Garza, H. H. P.; Kievit, E. W.; Schneider, G. F.; Staufer, U. Controlled, reversible, and nondestructive generation of uniaxial extreme strains (>10%) in graphene. *Nano Lett*. **2014**, *14*, 4107–4113.

(28) Dhakal, K. P.; Roy, S.; Jang, H.; Chen, X.; Yun, W. S.; Kim, H.; Lee, J.; Kim, J.; Ahn, J.-H. Local strain induced band gap modulation and photo-luminescence enhancement of multilayer transition metal dichalcogenides. *Chem. Mater*. **2017**, *29*, 5124–5133.

(29) Yang, S.; Wang, C.; Sahin, H.; Chen, H.; Li, Y.; Li, S.-S.; Suslu, A.; Peeters, F. M.; Liu, Q.; Li, J.; Tongay, S. Tuning the optical, magnetic, and electrical properties of ReSe2 by nanoscale strain engineering. *Nano Lett*. **2015**, *15*, 1660–1666.

(30) Palacios-Berraquero, C.; Kara, D. M.; Montblanch, A. R.-P.; Barbone, M.; Latawiec, P.; Yoon, D.; Ott, A. K.; Loncar, M.; Ferrari, A. C.; Atatüre, M. Large-scale quantum-emitter arrays in atomically thin semiconductors. *Nat. Commun*. **2017**, *8*, 15093.

(31) Kumar, S., Kaczmarczyk, A.; Gerardot, B. D. Strain-induced spatial and spectral isolation of quantum emitters in mono- and bilayer WSe2. *Nano Lett*. **2015**, *15*, 7567–7573.

(32) Tripathi, L. N.; Iff, O.; Betzold, S.; Dusanowski, Ł.; Emmerling, M.; Moon, K.; Lee, Y. J.; Kwon, S.-H.; Höfling, S.; Schneider, C.; Spontaneous emission enhancement in strain-induced WSe2 monolayer-based quantum light sources on metallic surfaces. *ACS Photonics* **2018**, *5*, 1919–1926.

(33) Yu, L.; Ruzsinszky, A.; Perdew, J. P. Bending Two-Dimensional Materials To Control Charge Localization and Fermi-Level Shift. *Nano Lett*. **2016**, *16*, 2444−2449.

(34) Perdew, J. P.; Burke, K.; Ernzerhof, M. Generalized Gradient Approximation Made Simple. *Phys. Rev. Lett.* **1996**, *77*, 3865.

(35) Sun, J.; Ruzsinszky, A.; Perdew, J. P. Strongly Constrained and Appropriately Normed Semilocal Density Functional. *Phys. Rev. Lett*. **2015**, *115*, 036402.

(36) Aschebrock, T.; Kümmel, S. Ultranonlocality and accurate band gaps from a meta-generalized gradient approximation. *Phy. Rev. Res*. **2019**, 1, 033082.

(37) Neupane, B.; Tang, H.; Nepal, N. K.; Adhikari, S.; Ruzsinszky, A. Opening band gaps of low-dimensional materials at the meta-GGA level of density functional approximations. *Phys. Rev. Mater*. **2021**, *5*, 063803.

(38) Krukau, A. V.; Vydrov, O. A.; Izmaylov, A.r F.; Scuseria, G. E. Influence of the exchange screening parameter on the performance of screened hybrid functionals. *J. Chem. Phys.* **2006**, *125*, 224106.

(39) Kresse, G.; Furthmüller, J. Efficient iterative schemes for ab initio total-energy calculations using a plane-wave basis set. *Phys. Rev. B* **1996**, *54*, 11169.

(40) Deslippe, J.; Samsonidze, G.; Strubbe, D. A.; Jain, M.; Cohen, M. L.; Louie, S. G. BerkeleyGW: A Massively Parallel Computer Package for the Calculation of the Quasiparticle and Optical Properties of Materials and Nanostructures. *Comput. Phys. Commun*. **2012**, *183*, 1269.

(41) Hybertsen, M. S.; Louie, Steven G. Electron correlation in semiconductors and insulators: Band gaps and quasiparticle energies. *Phys. Rev. B* **1986**, *34*, 5390.

(42) Pan, H.; Zhang, Y.-W. Edge-dependent structural, electronic and magnetic properties of MoS2 nanoribbons. *J. Mater. Chem*. **2012**, *22*, 7280.

(43) Li, Y.; Zhou, Z.; Zhang, S.; Chen, Z. MoS2 Nanoribbons: High Stability and Unusual Electronic and Magnetic Properties. *J. Am. Chem. Soc.* **2008**, *130*, 16739–16744.

(44) Refaely-Abramson, S.; Qiu, D. Y.; Louie, S. G.; Neaton, J. B. Defect-Induced Modification of Low-Lying Excitons and Valley Selectivity in Monolayer Transition Metal Dichalcogenides. *Phys. Rev. Lett*. **2018**, *121*, 167402.

(45) Trauzettel, B.; Bulaev, D. V.; Loss, D.; Burkard, G. Spin qubits in graphene quantum dots. *Nat. Physics* **2007**, *3*, 192–196.

(46) Remskar, M.; Mrzel, A.; Skraba, Z.; Jesih, A.; Ceh, M.; Demsar, J.; Stadelmann, P.; Levy, F.; Mihailovic, D. Self-Assembly of Subnanometer-Diameter Single-Wall MoS2 Nanotubes. *Science* **2001**, *292*, 479−481.

(47) Strojnik, M.; Kovic, A.; Mrzel, A.; Buh, J.; Strle, J.; Mihailovic, D. MoS2 nanotube field effect transistors. *AIP Advances* **2014**, *4*, 097114.

Table 1. The quasiparticle gap E_g, the energies of exciton forming the lowest energy peak in the absorption spectra E_{A} (for spin singlet), $E_{\mathrm{A}}^{\mathrm{triplet}}$ (for spin triplet), the binding energy of this exciton E_b (for spin singlet), and the spin singlet-triplet split $\Delta^{\mathrm{S-T}}$ for $A12MoS_2$ and $A13MoS_2$ nanoribbons under different bending curvature radii. E_g is from GW calculations. $E_b = E_g - E_{\mathrm{A}}$ and $\Delta^{\mathrm{S-T}} = E_{\mathrm{A}} - E_{\mathrm{A}}^{\mathrm{triplet}}$. Energy unit in eV.

	$A13MoS_2$				
	E_g	E_{A}	E_b	$E_{\mathrm{A}}^{\mathrm{triplet}}$	$\Delta^{\mathrm{S-T}}$
$R = \infty$ (flat)	1.98	0.57	1.41	0.35	0.22
$R = 13$ Å	1.91	0.50	1.41	0.30	0.20
$R = 9$ Å	1.88	0.50	1.38	0.30	0.20
$R = 6$ Å	1.47	0.33	1.14	0.28	0.05
	$A12MoS_2$				
	E_g	E_{A}	E_b	$E_{\mathrm{A}}^{\mathrm{triplet}}$	$\Delta^{\mathrm{S-T}}$
$R = \infty$ (flat)	2.06	0.59	1.47	0.37	0.22
$R = 14$ Å	1.89	0.49	1.40	0.30	0.19
$R = 10$ Å	1.85	0.45	1.40	0.26	0.19
$R = 7$ Å	1.66	0.41	1.25	0.24	0.17

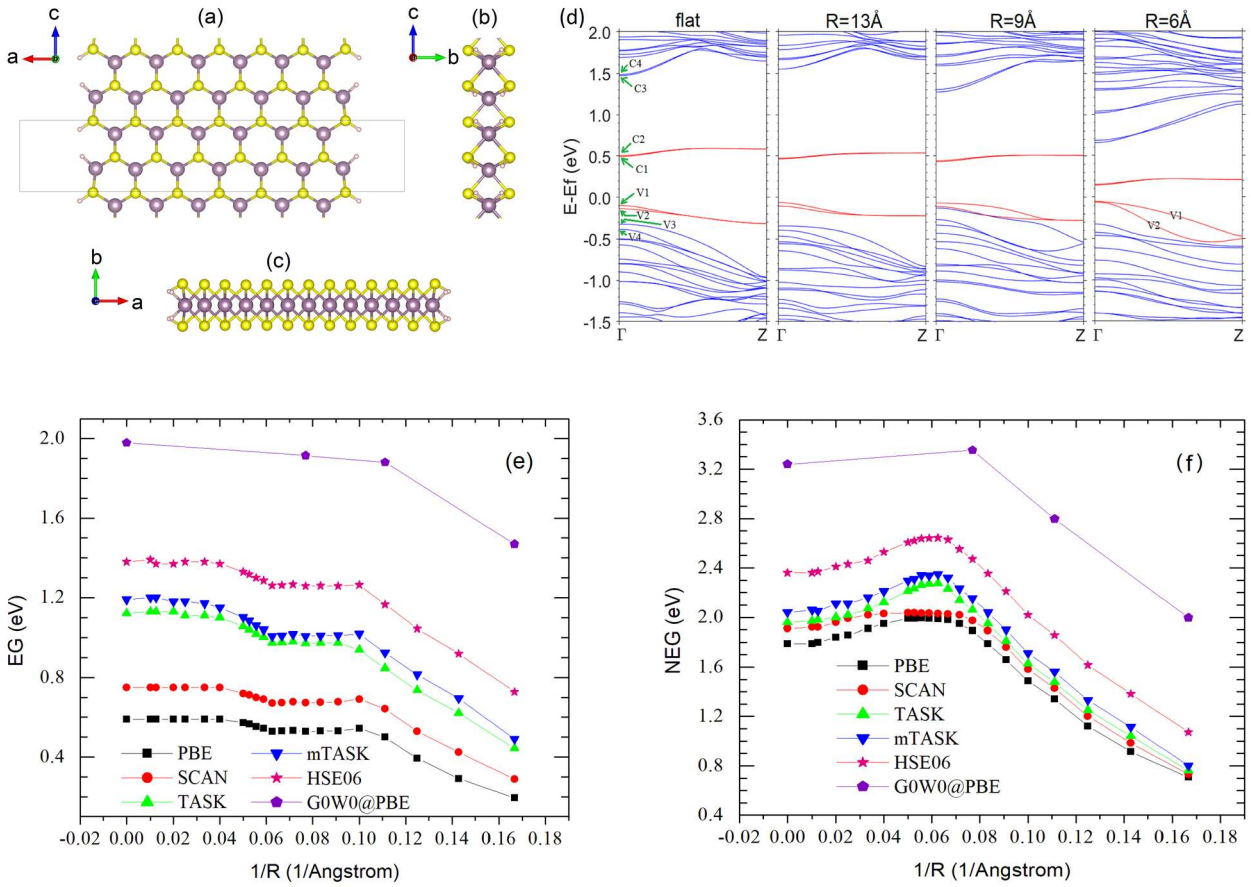

Figure 1. The structure of hexagonal armchair monolayer MoS_2 nanoribbon A$n$$MoS_2$ with n=13 and its band structure and gap evolutions with the bending curvature radius. (a) structure view along axis y. The supercell vectors a, b and c are aligned with axes x, y and z, respectively. The box outlines the periodical unit of the nanoribbon along axis z. The two hydrogen-passivated armchair edges are on the left and right sides. The view along axis x is in (b) and along axis z is in (c). The blue balls represent Mo atoms, the yellow ones for S atoms, and small white ones for H atoms. The band structure evolution with the bending curvature radius is in (d). The conduction bands C1, C2, C3… are numbered upwards, while the valence bands V1, V2, V3… are numbered downwards. The four bands near the Fermi level are plot in red, while others are in blue. The edge band gaps (EG) in (e) and non-edge band gaps (NEG) in (f) as a function of bending curvature κ ($\kappa = 1/\mathrm{R}$) for the A13MoS_2 nanoribbon are shown. The results from PBE,[34] SCAN,[35] TASK,[36] mTASK,[37] HSE06[38] and G_0W_0[40,41] are shown, and have nearly the same trend. EG is defined as the energy difference between C1 and V1 at the Γ point, and NEG as that between C3 and V3. When V1 and V2 are merged into the valence band continuum, NEG is the difference between C3 and V1.

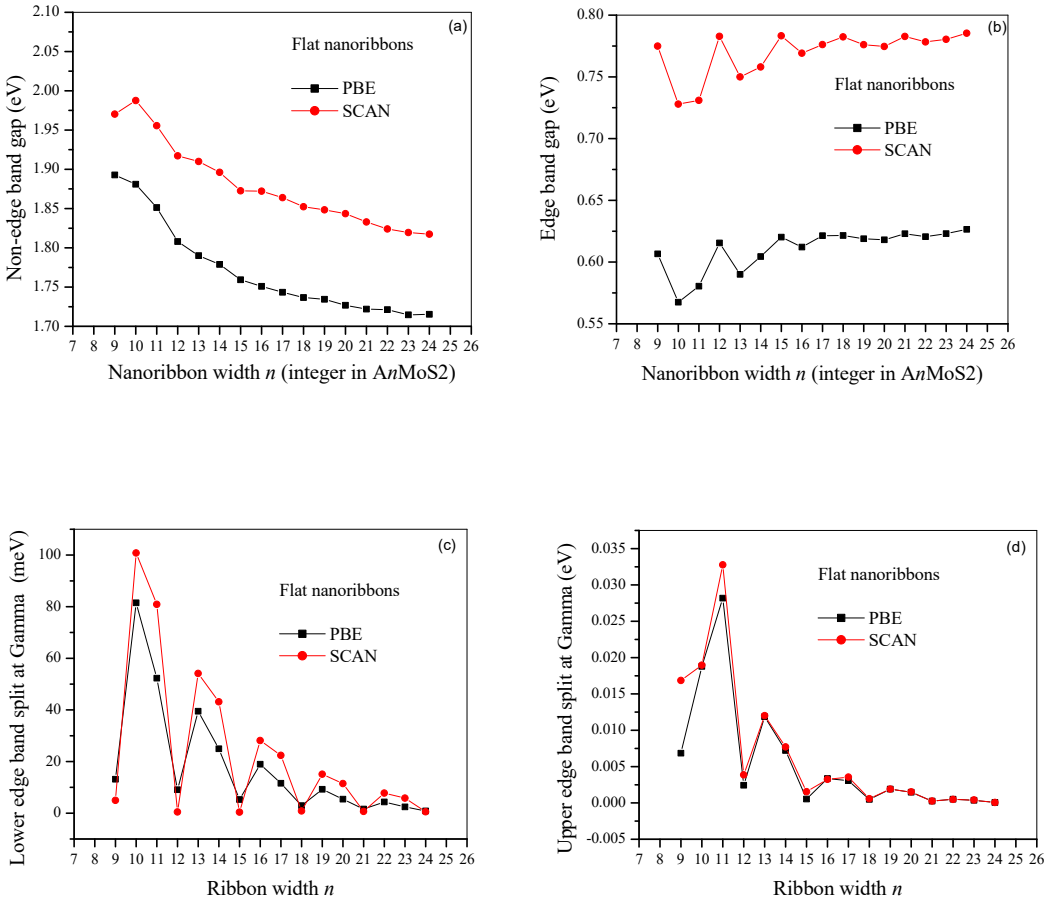

Figure 2. The non-edge band gap (NEG) in (a), the edge band gap (EG) in (b), the non-degenerate splits of edge bands ΔE_{V} (lower edge band split) in (c) and ΔE_{C} (upper edge band split) in (d) of flat nanoribbons AnMoS$_2$ with n from 9 to 24, as the function of ribbon width, obtained with the PBE and SCAN functionals. NEG approximately shows a monotonic decrease trend with n, while EG shows an oscillating feature with a period $\Delta n = 3$. $\Delta E_{\mathrm{C}} = E_{\mathrm{C2}} - E_{\mathrm{C1}}$, defined as the energy difference between C2 and C1 at the Γ point (see Figure 1d), and $\Delta E_{\mathrm{V}} = E_{\mathrm{V1}} - E_{\mathrm{V2}}$, the energy difference between V1 and V2 at the Γ point. For flat nanoribbons AnMoS$_2$ with n = 9, 12, 15, 18, 21, and 24 (i.e., $n = 3p$, where p is an integer), both ΔE_{C} and ΔE_{V} are minimal, showing nearly degenerate edge bands. The flat nanoribbons with other n values show non-degenerate edge bands.

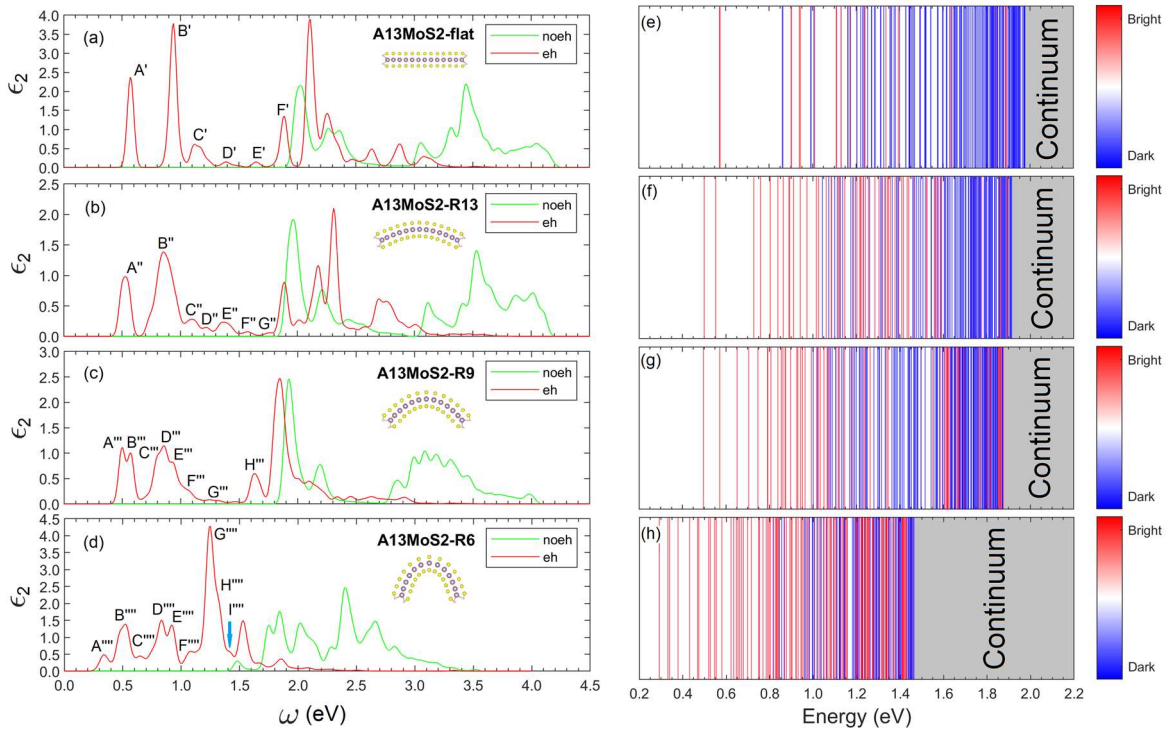

Figure 3. The optical absorption spectra and the corresponding exciton spectra of $A13MoS_2$ nanoribbon under different bending curvatures. The optical absorption spectra are plotted as the imaginary part of the dielectric function as a function of photon energy for curvature radii (a) $R = \infty$ (flat), (b) $R = 13$Å, (c) $R = 9$Å, and (d) $R = 6$Å. Red curves represent the GW+BSE results with electron-hole (eh) interactions and the green ones are for the results without eh interactions, both with constant broadening of 26meV. Labels in (a)-(d), i.e., A′, A″, A‴, A⁗, B′, etc. represent different peaks. Inset graphs in (a)-(d) show the structures of bent nanoribbons. The exciton spectra show the energy positions of exciton sates for curvature radii (e) $R = \infty$ (flat), (f) $R = 13$Å, (g) $R = 9$Å, and (h) $R = 6$Å. Bright (dark) exciton states are represented by red (blue) lines.

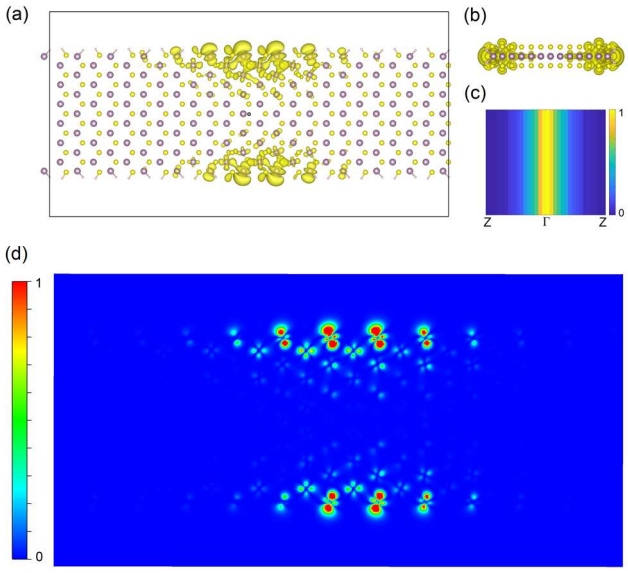

Figure 4. The exciton state forming peak A′ (Figure 3a) in real space (a) top view, (b) side view, and in k space (c). The hole (black spot in (a)) is located at the center of the ribbon and near a Mo atom. The isosurface contour of the modulus squared exciton wavefunction is shown in (a) and (b). The profile (arbitrary unit) of the modulus squared exciton wavefunction in k space is shown in (c), showing it is around the Γ point, and in real space is shown in (d), showing the electron in the exciton is mainly located on the edge Mo atoms. The plots for other exciton states are in Figures S11-S20(Supporting Information).

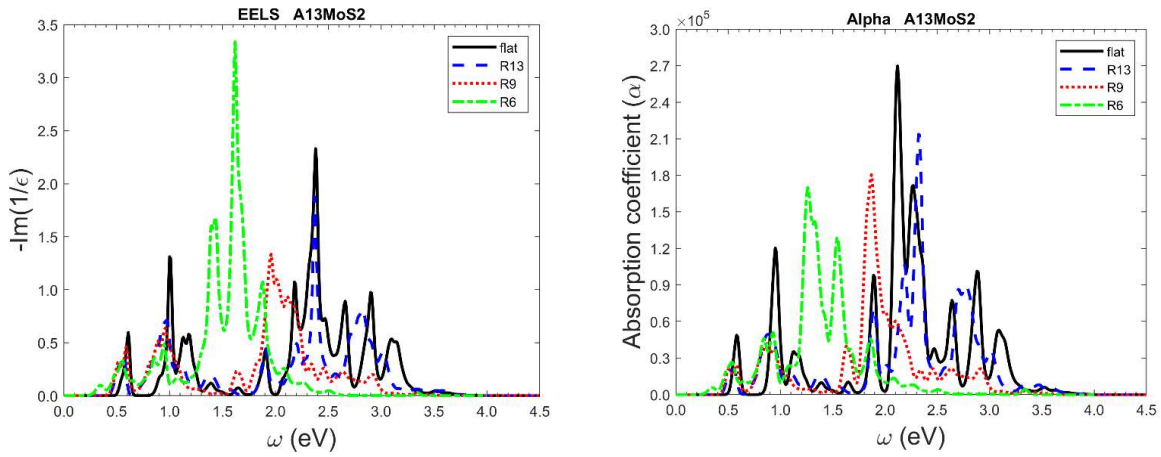

Figure 5. The electron energy loss spectrum (EELS) and absorption coefficient of $A13MoS_2$ nanoribbon under different bending curvatures. EELS is calculated as the imaginary part of $-1/(\varepsilon_1 + i\varepsilon_2)$. The absorption coefficient α is calculated as $\omega\ \varepsilon_2/(nc)$ (cm^{-1}, Gaussian unit), where $n = \sqrt{(\sqrt{\varepsilon_1^2 + \varepsilon_2^2} + \varepsilon_1)/2}$ is the refractive index and c is the speed of light in vacuum. R13 represents the bending curvature radius $R = 13$Å and so on. The plots for the $A12Mos_2$ nanoribbon are in Figure S25 (Supporting Information).